

# Porous SnS Nanorods/Carbon Hybrid Materials as Highly Stable and High Capacity Anode for Li-Ion Batteries

Junjie Cai, Zesheng Li, and Pei Kang Shen\*

The State Key Laboratory of Optoelectronic Materials and Technologies, and Guangdong Province Key Laboratory of Low-Carbon Chemistry & Energy Conservation, School of Physics and Engineering, Sun Yat-sen University, Guangzhou, 510275, PR China.

## Supporting Information

**ABSTRACT:** A new solid–liquid–gas–solid (SLGS) growth strategy has been exploited to prepare porous SnS nanorods directly on carbon hybrid nanostructure by using a sulfur-containing resin (s-resin) laden with crystalline SnO<sub>2</sub> nanoparticles and subsequent calcination promoted the development of porous SnS nanorods growing on carbon. As an anode material in Li-ion batteries (LIBs), SnS nanorods/C hybrid materials show highly stable and high capacity retention rate, which suggest that the novel hybrid materials have alluring prospect for electrochemical energy storage applications.

**KEYWORDS:** SnS nanorods, hybrid materials, Li-ion batteries, energy storage, resin



## INTRODUCTION

During the past decade, one-dimensional (1D) nanostructures such as nanowires, nanorods, nanobelts and nanoneedles, have become one of the most highly energized research areas because of their unique structures, novel properties, and great potential applications.<sup>1–3</sup> It is generally accepted that 1D nanostructures are ideal systems for exploring a large number of novel phenomena at the nanoscale and investigating the dependence of electrical and thermal transport or mechanical properties on dimensionality and size reduction.<sup>4,5</sup> The 1D nanomaterials are also regarded as both interconnects and functional building blocks in fabricating nanodevices.<sup>6,7</sup>

Nanomaterials with porous structures are expected to play an important role in a wide variety of applications as gas sensors, catalysts and energy storage.<sup>8–10</sup> In particular, one of the most exciting potential applications of these porous materials is considered to be used as electrode materials for Li-ion batteries. Generally, porous materials with a high surface area which may permits electrolyte percolation into active materials and hence efficiently use of electrode material, thereby result in a higher capacity. For instance, the capacity of the electrode with porous nanostructure has been observed to be higher than that of nonporous powders.<sup>11–14</sup> Recently, the investigations on the synthesis and characterization of porous 1D nanomaterials have been carried out. Porous 1D nanostructure can be fabricated using a number of advanced techniques, such as template-based techniques, hydrothermal method, noncovalent self-assembly and coordination modulation growth.<sup>15–17</sup> However, further development of these techniques into practical routes to large quantities of porous 1D nanostructures with accurate size, shape control, rapidly and reasonably low costs, are still great challenges.

As an important IV–VI semiconductor, tin(II) sulphide (SnS) with orthorhombic structure, has attracted considerable

attention because of its unique chemical and physical properties.<sup>18–20</sup> Currently, another tin sulphide (SnS<sub>2</sub>) have been widely studied as anode materials for LIBs,<sup>21,22</sup> however, only a few efforts devoted to the investigation of SnS as anode material for Li-ion battery.<sup>23,24</sup> To the best of our knowledge, SnS shows higher theoretical specific capacity than SnS<sub>2</sub> due to its lower molecular weight, suggesting that SnS is a promising anode materials. Although SnS shows high initial discharge capacities, the poor cycle stability originated from serious volume expansion during charge/discharge processes is still a hinder for its practical application. To solve this issue, some approaches have been proposed. For example, Lou and Li<sup>25–27</sup> reported that they made active materials into effective hybrid nanostructures to significantly improve the electrochemical performance of the electrode. As above discussion, the porous 1D hybrid nanostructures are also considered to be the optimized architectures for electrochemical electrodes because of their higher surface-to-volume ratio, better mass transport capability, and relatively lower volume change during the charge/discharge processes compared with the bulk counterparts.<sup>28–30</sup>

Recently, well-designed SnS nanomaterials were synthesized by various methods, such as thermal decomposition<sup>31</sup> and chemical vapor deposition.<sup>32</sup> Panda et al.<sup>33</sup> reported that a gas–solid reaction approach to grow SnS nanowires on the tin metal surface by exposing to a H<sub>2</sub>S atmosphere. Nevertheless, simply producing SnS nanorods (NRs) on carbon substrates and its application as anode materials for LIBs has never been reported yet. In this paper, we first report the preparation of porous 1D SnS nanorods directly on carbon with large areas via a new

Received: May 16, 2012

Accepted: July 24, 2012

Published: August 2, 2012

solid–liquid–gas–solid (SLGS) growth strategy. In briefly, a sulfur-containing resin (s-resin) laden with crystalline  $\text{SnO}_2$  nanoparticles as precursor was prepared by using solvothermal method and then an easier thermal solid-state technique was selected to promote the development of porous SnS NRs/carbon hybrid materials. In our strategy, the resin plays a key role because of its unique macroreticular structure and sulfonic acid groups can absorb the tin cations and act as the nucleation sites for growing  $\text{SnO}_2$  nanocrystals. In addition, the carbon and sulfur source were all provided by pyrolysis of the s-resin and no need to extra volatile precursors. Therefore, SLGS strategy is relatively simple and can be scaled to mass production compared with conventional VLS or VS growth modes for 1D nanostructures.

## EXPERIMENTAL SECTION

**Synthesis of Porous SnS Nanorods on Carbon.** In a typical synthesis, 4 mmol of  $\text{SnCl}_2 \cdot \text{H}_2\text{O}$  were mixed with 2 g of Amberlite 200 resin in ethanol, followed by solvothermal synthesis at 220 °C for 12 h. The  $\text{SnO}_2$  nanoparticles with a mean diameter of 12 nm were coated onto the resin, which could be collected by centrifugation once the solution had cooled down. Then, heat it in  $\text{N}_2$  atmosphere at 800 °C for 1 h, the  $\text{SnO}_2$ /s-resin could be transformed into SnS NRs/carbon. The controlled experiment on resin-derived carbon and higher SnS content samples were attained by using 0 and 8 mmol  $\text{SnCl}_2 \cdot 2\text{H}_2\text{O}$ , respectively.

**Characterization and Electrochemical Measurement.** The X-ray powder diffraction (XRD) measurements were carried out on a D/Max-III (Rigaku Co.Ltd., Japan) using Cu K $\alpha$  radiation and operating at 40 kV and 30 mA. The morphologies and constituent content were observed by a Quanta 400 TF scanning electron microscopy (SEM) (Philips Co.Ltd., Holland) and energy-dispersive X-ray spectroscopy (EDS) (Oxford Co.Ltd., England) analysis. Transmission electron microscopy (TEM) investigations were carried out on a JEOL JEM-2010 (JEOL Ltd., Japan) at 200 kV. An ICP-AES instrument (ELAN 6100,401 PerkinElmer) was used to determine the SnS content in hybrid materials.

For the electrochemical measurements, the as-prepared porous SnS NRs/carbon samples were mixed with acetylene black and polyvinylidene fluoride (PVDF) at a weight ratio of 80:10:10 in N-methyl-2-pyrrolidene (NMP) solution. The mixed ink was coated on a copper foil and dried in vacuum oven at 120 °C for 10 h and was pressed and then cut into 1.54 cm<sup>2</sup> disk. The 2032 coin-type cells were assembled in an argon-filled glovebox using pure lithium as the anode, 1 M  $\text{LiClO}_4$  in ethylene carbonate (EC)/dimethylcarbonate (DMC) (1:1) as the electrolyte and microporous membrane (Celguard 2400, USA) as the separator. The cells were galvanostatically charged and discharged between 0.01 and 2 V versus lithium at room temperature on a program-controlled test system (Shenzhen Neware Battery Co., China). The cyclic voltammetric and electrochemical impedance spectroscopy measurements were performed on an IM6e electrochemical workstation (Zahner-Elektrik, Germany).

The specific capacity of the porous SnS NRs/carbon composite was calculated based on the whole weight of the hybrid materials and the specific capacity of porous SnS NRs in the hybrid materials which can be defined as the following expression

$$\text{specific capacity of SnS NRs} = (C_{\text{SnS/C}} - C_{\text{carbon}})/W$$

where  $C_{\text{SnS/C}}$  and  $C_{\text{carbon}}$  are the specific capacities of the porous SnS NRs hybrid materials and carbon in the hybrid materials, respectively.  $W$  is the weight ratio of SnS NRs in the hybrid materials.

## RESULTS AND DISCUSSION

The crystallographic structure and phase purity of the as-prepared samples are examined by X-ray powder diffraction (XRD) as shown in Figure 1. The precursor sample ( $\text{SnO}_2$ /s-resin complex) before annealing was expectedly contained

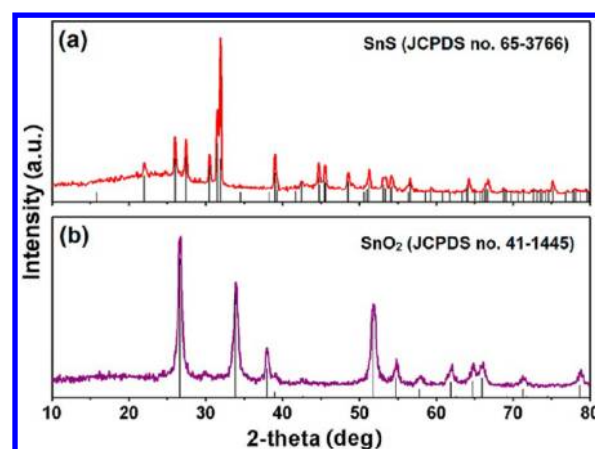


Figure 1. XRD patterns of (a) SnS NRs/carbon and (b)  $\text{SnO}_2$ /s-resin precursor.

$\text{SnO}_2$  component as evidenced by the clear diffraction peaks from the tetragonal  $\text{SnO}_2$  (JCPDS no. 41–1445). After controlled annealing at 800 °C in nitrogen, the tetragonal  $\text{SnO}_2$  phase can be readily changed into pure SnS phase (JCPDS no. 65–3766). The signals from the  $\text{SnO}_2$  entirely disappear and no signals from possible impurities such as metal Sn were detected in the annealed sample. Along with the conversion from resin to carbon, SnS/carbon hybrid materials were prepared in the synchronic thermal solid-state synthesis.

The morphologies of the SnS NRs/carbon hybrid architectures were observed by scanning electron microscopy (SEM). Meanwhile, the chemical composition of the sample was determined by the energy-dispersive X-ray spectroscopy (EDS) attached to SEM. Figure S1a in the Supporting Information shows a representative SEM image of the carbon-supported SnS NRs. The diameters of the NRs are in the range of 50 to 200 nm and the length can be determined up to 2.5  $\mu\text{m}$  despite their overlapped shapes. The results of the linear SEM-EDS crossing several SnS NRs (see Figure S1b in the Supporting Information) indicated that the C, O, S and, Sn elements are synchronously distributed on the NRs within the line scan range. There is a possibility of C and O elements coexisting in the SnS matrix, arising from the gas carbon diffusion process (e.g.,  $\text{CO}_2$ ). In addition, the EDS mapping images (Figure 2a) revealed that most of these SnS NRs are rooted in the carbon substrates. The corresponding composition and element contents of this region are also presented in images b and c in Figure 2, respectively. From the EDS result, we can see that the ratio of tin to sulfur elements is not exactly equal to 1:1. The reason is that we always kept s-resin excessive in our experiment to guarantee enough S element react with tin to form pure SnS. As a result, the excessive sulfur and oxygen elements will still exist in the s-resin derived carbon which led to the EDS result. To obtain the quantitative result of the mass percentage of SnS in the composite, plasma-atomic emission spectrometry (ICP-AES) analysis technique were carried out and the content of SnS were determined to be 21.7 wt % when using 4 mmol of  $\text{SnCl}_2 \cdot \text{H}_2\text{O}$  as starting material. And more detailed structures with regard to the supported SnS NRs can be found in Figures S2 and S3 in the Supporting Information.

The porous textures and geometrical structure of the as-prepared SnS NRs are further elucidated by transmission electron microscopy (TEM) as displayed in Figure 3. It is agreement with the above SEM findings that a number of well-



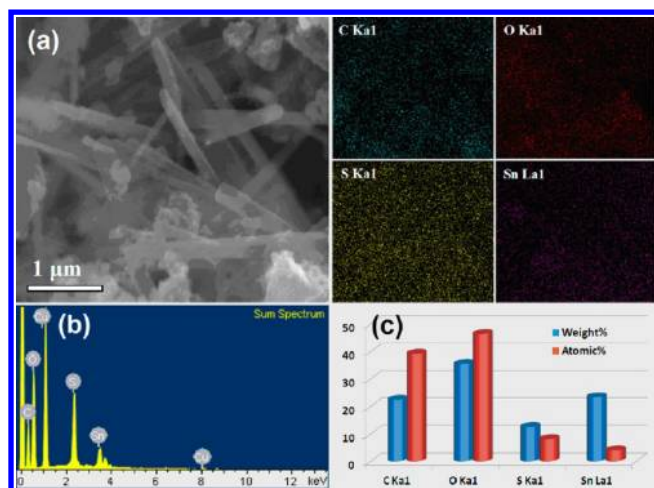


**Figure 2.** (a) SEM-EDS mapping images, (b) EDS pattern, and (c) the corresponding element contents of the SnS NRs/carbon hybrid materials.

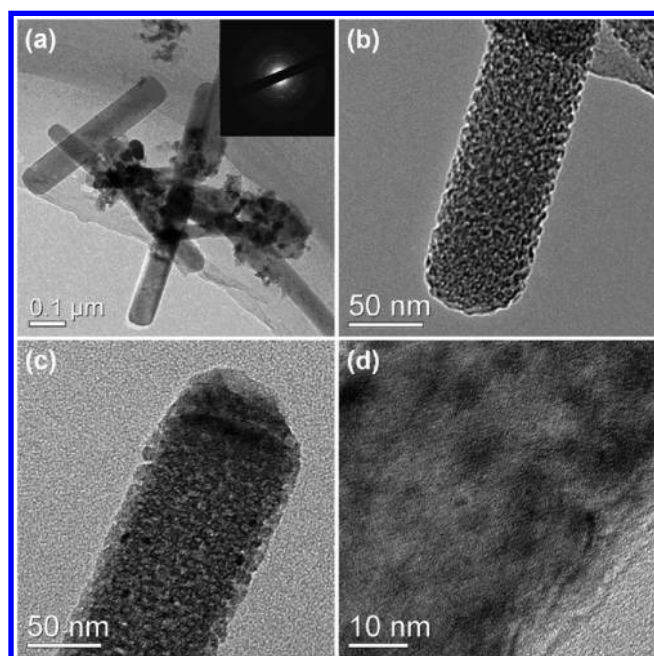


**Figure 3.** (a–c) TEM and (d) HR-TEM images of the SnS nanorods; inset in image a is the selective area electron diffraction (SAED) pattern.

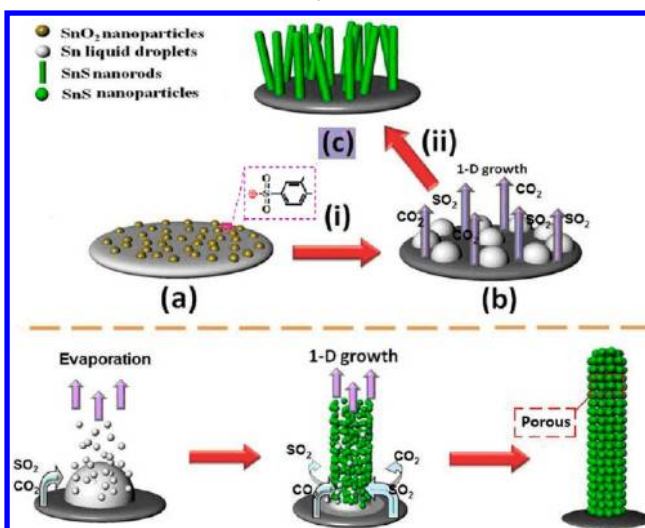
defined NRs can be seen from a lower magnification image (Figure 3a). These NRs have uniform diameters throughout their whole lengths. The ring patterns of the selected-area electron diffraction (SAED) image (see the inset of the Figure 3a) are good indicative of their polycrystalline structures of our SnS NRs. The blurred ring patterns can be derived from the amorphous carbon phase. It is interesting to note that highly porous structures of the NRs are distinctively demonstrated by the higher magnification images in images b and c in Figure 3. Obviously, large quantities of the pore defects are widely distributed on the surface of SnS NRs, the yield of the pore defect mainly rely on the assembly of SnS nanoparticles and pyrolysis of s-resin and the release of gases ( $\text{CO}_2$ ,  $\text{SO}_2$ ) during the calcination process. The high-resolution (HR) TEM image (see Figure 2d) also suggests that the porous 1D textures might result from the self-assembly of numerous SnS nanoparticles,

which could be consolidated by the latent carbon component. As a whole, our work demonstrated a sort of new, interesting, porous 1D nanostructured architectures over previous reports.<sup>8–10</sup>

The vapor–liquid–solid (VLS)<sup>34,35</sup> and solution–liquid–solid (SLS)<sup>36–38</sup> growth mechanisms have been widely applied to prepare various continuous 1D crystalline nanostructures via vapor- and solution-state routes, respectively. In order to develop new functionality of the 1D nanomaterials, the rational design and synthesis of porous nanostructures of these materials has been continuously pursued.<sup>8–14</sup> Very recently, we reported the fabrication of unique porous crystalline  $\text{Co}_3\text{O}_4$  nanobelts by a thermal decomposition from the precursor  $\text{Co}(\text{OH})_2$  nanobelts based on the topotactic conversion route.<sup>39</sup> Herein, we endeavor to present another new growth mechanism for synchronous synthesis of porous 1D nanomaterials.

Scheme 1 illustrates a formation process of the porous SnS NRs with the present synthesis route. In brief, the 1D growth

**Scheme 1. Schematic of the 1D Growth Process of Porous SnS NRs via SLGS Growth Strategy:** (a)  $\text{SnO}_2$ /s-Resin Precursor Complexes, (b) Intermediate State Complexes, and (c) SnS NRs/Carbon Hybrid Materials<sup>a</sup>



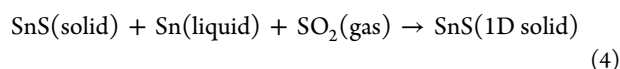
<sup>a</sup>The bottom shows the detailed development of 1D porous textures.

process consists of two main steps: (i) intermediate state and (ii) NRs developing state. The intermediate state includes the formation of the Sn liquid droplets resulted from  $\text{SnO}_2$  carbothermal reduction and the production of  $\text{SO}_2$  gas by thermal decomposition of sulfonic acid groups ( $\text{R-SO}_3^+$ ) during the heating treatment (see eqs 1 and 2).



In the following processes, the  $\text{SO}_2$  gas first diffuses to Sn liquid droplet to form SnS liquid–solid interface and the 1D growth of the SnS NRs initiates at the liquid–solid interface, and then the continuous 1D growth of the SnS NRs which consumes the Sn liquid droplet, leading to the completion of the SnS NRs assembly (see eqs 3 and 4).





Synchronously, the produced  $\text{CO}_2$  gas from thermal decomposition of resin could easily penetrate into the generated liquid–solid interface in the developing state of SnS NRs, which provides appropriate cavities responding for their porous textures (see the bottom in Scheme 1). As a result, the porous SnS NRs/carbon hybrid materials were obtained by this simple thermal solid-state synthesis.

Interestingly, when doubling the loading of  $\text{SnO}_2$ , free-standing SnS NRs with high density (38.2 wt % SnS in the composite) can be produced as shown in Figure 4. High  $\text{SnO}_2$

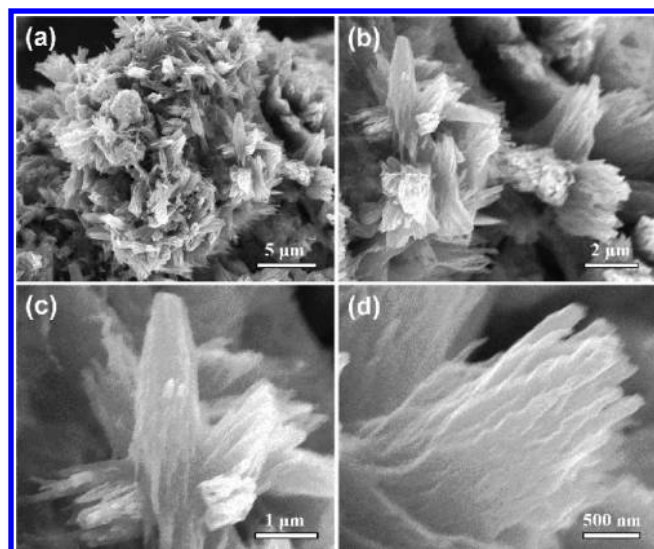


**Figure 4.** SEM images of the free-standing SnS NRs (38.2 wt % SnS in the composite).

content means that the resin surface was more closely covered by  $\text{SnO}_2$  nanoparticles. Large accumulation of  $\text{SnO}_2$  at a small area which led to SnS NR roots joint together and formation of sheet like SnS during the NRs growth process. However, we can still distinguish the top of SnS present a nanowhisker structure in a higher magnification picture (Figure 4d). Obviously, this nanostructure is a variant of SnS NRs. We hereby call this unique  $\text{SnO}_2$ /s-resin derived 1D growth mode a solid–liquid–gas–solid (SLGS) process. This could be an interesting extension of the VLS and SLS methods with an additional process to achieve attractive 1D nanostructures. It is noteworthy that this should be a new and general mechanism for the growth of 1D nanostructures of low-melting-point metal sulphides (e.g., lead, bismuth and indium sulfides). Especially, in comparison to prevailing methods, including hydrothermal synthesis and vapor deposition, for the synthesis of 1D nanostructures, the thermal solid-state technique has more advantages concerning its practicability, low cost, and high efficiency, which are beneficial for scalable synthesis and practical applications.

To investigate the anodic performance of the as-prepared porous SnS NRs/carbon electrodes, we first implemented cyclic voltammograms (CVs). Figure 5a shows the CV curves for the first 2 cycles at a scan rate of 0.5 mV/s in the potential range from 0.0 to 2.0 V, which presents the same electrochemical reaction pathway of SnS component as discussed in the literature.<sup>40</sup> Typically, two reduction peaks were observed in

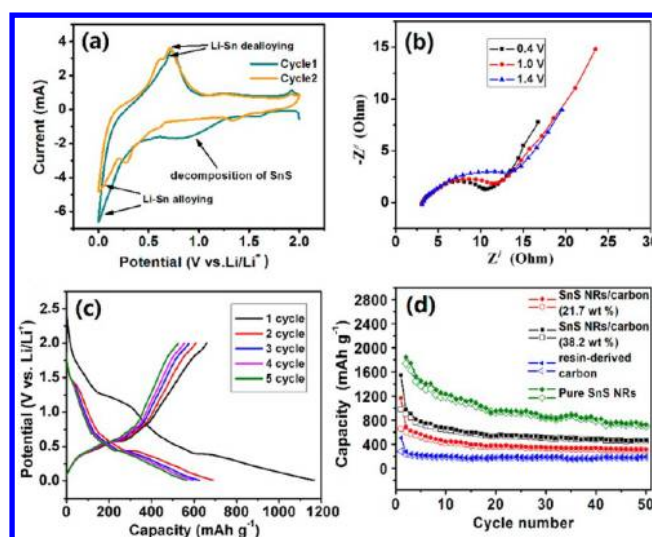
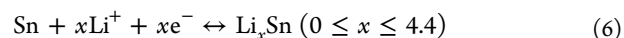
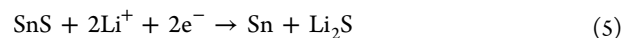


**Figure 5.** (a) Cyclic voltammograms, (b) Nyquist plots from EIS, (c) charge/discharge curves of the SnS NRs/carbon, and (d) discharge–charge cycling performance of the different samples.

the cathodic scans, the first peak at around 1.3–0.6 V is ascribed to irreversible decomposition of SnS to Sn and  $\text{Li}_2\text{S}$ , and the second dominant peak between 0.6 and 0.0 V is known to arise from the formation of  $\text{Li}_x\text{Sn}$  alloys. The  $\text{Li}^+$  insertion/deinsertion mechanism could be proposed as



Electrochemical impedance spectroscopy (EIS) measurement of the as-prepared electrodes was conducted in a frequency range of  $1 \times 10^5$  to  $1 \times 10^{-2}$  Hz and at the a.c. amplitude of 5 mV. Nyquist plots obtained from EIS of the SnS NRs/carbon samples are shown in Figure 5b. Three different controlled potential of 1.4 V, 1.0 and 0.4 V were selected to study the internal resistance of the electrodes during the  $\text{Li}^+$  intercalation process. It is apparent that the sample has lower initial interfacial resistance (the diameter of semicircle at high to middle frequency) and higher charge transfer rate (the slope of inclined line at middle to low frequency) in each potential. As the  $\text{Li}^+$  insertion progressed, expressly, the internal resistance of the electrodes was decrease from 20 to 12  $\Omega$ . The excellent conductivity was attributed to the unique 1D nanostructures grow on carbon substrate, which can improve electrons transfer and decreased electrical resistivity.

Figure 5c shows the galvanostatic charge/discharge (GCD) curves of the sample with low SnS content (21.7 wt %) for the first 5 cycles at a current density of 50 mA/g in the potential range from 0.01 to 2.0 V. It is noted that the first discharge profile has two relevant plateau regions at about 1.3–0.6 V and the result was confirmed by CV analysis. From the second cycle, the discharge profiles indicate relatively constant lithiation and delithiation processes for the SnS NRs/carbon electrode.

Figure 5d shows the capacity and cycling performance of the high content SnS (38.2 wt %) and low content SnS (21.7 wt %) NRs/carbon compared with resin-derived carbon electrodes at a current rate of 50 mA/g. Surprisingly, despite only 21.7 and 38.2% of SnS components in the hybrid materials, the SnS NRs/carbon electrode show a high initial capacity of 1167 mA h/g and 1538 mA h/g, respectively. Considering the theoretical



capacity and the reversible capacity of SnS are 1134 and 782 mA h/g calculated by eqs 5 and 6, the specific discharge capacity of SnS NRs/carbon hybrid materials should not exceed 1134 mA h/g. However, the high surface area of the low temperature carbonized carbon<sup>41</sup> and porous structure of SnS NRs directly led to the unusual high initial capacity because of the electrolyte decomposition and formation of solid electrolyte interphase (SEI) layer on the large surface of them in the first discharge.<sup>42</sup> At the end of 50th charge–discharge cycles, a reversible discharge capacity of 466 and 308 mA h/g was still retained for the 38.2 and 21 wt % SnS NRs/carbon materials, whereas only 189 mA h/g was retained for the resin-derived carbon. In the following discussion, the 38.2 wt % SnS NRs/carbon composite will be taken as example to illustrate that these data show a significant improvement of the electrode by making some conversion. First, according to the theoretical value of SnS (1134 mA h/g) and the reversible capacity of carbon (~200 mA h/g) from our test result, the 38.2 wt % SnS NRs/carbon composite should have a total capacity contribution of about 557 mAh/g. In other word, a reversible discharge capacity of 466 mA h/g of 38.2 wt % SnS NRs/carbon composite is equal to 84% of its theoretical reversible capacity after 50 cycles. Second, if deduct the capacity contribution of resin-derived carbon, the specific capacity of pure porous SnS NRs is about 696 mA h/g after 50 cycles, which is very close to 90% of its theoretical reversible capacity (782 mA h/g). The high capacity retention rate of porous 1D SnS in our study is significantly better than the SnS nanopowders which have been reported.<sup>28–30</sup> All evidence demonstrate that the porous 1D SnS NRs/carbon hybrid nanostructure is an effective way to enhance the electrochemical performance for Li-ion batteries.

In summary, the porous SnS NRs directly on carbon hybrid nanostructure were successfully prepared by a new solid–liquid–gas–solid (SLGS) growth strategy. Our strategy is relatively simple and can be scaled up for a practical application compared with traditional methods for 1D nanostructures, such as VLS or VS growth mode. It is a significant improvement for preparing 1D nanostructures and we believe that the SLGS growth strategy is probably a general method to prepare 1D metal sulphides for low-melting-point metal. In our study, such porous SnS NRs/carbon hybrid nanostructure exhibited improved reversible capacity and cycling performance. The enhanced electrode performance could be attributed to both the existence of the carbon species and the unique architecture. Because of the simple growth strategy and good electrode performance, we suggest that the SnS NRs/carbon hybrid materials as anode show alluring prospect for electrochemical energy storage.

## ■ ASSOCIATED CONTENT

### ■ Supporting Information

Synthesis details and more physical characterization. This material is available free of charge via the Internet at <http://pubs.acs.org>.

## ■ AUTHOR INFORMATION

### Corresponding Author

\*E-mail: [stsspk@mail.sysu.edu.cn](mailto:stsspk@mail.sysu.edu.cn).

### Notes

The authors declare no competing financial interest.

## ■ ACKNOWLEDGMENTS

This work was supported by the link project of the National Natural Science Foundation of China and Guangdong Province (U1034003) and the State Key Laboratory of Optoelectronic Materials and Technologies (2010-ZY-4-4, 2010-ZY-4-7).

## ■ REFERENCES

- (1) Wang, X.; Yan, J.; Zhou, Y.; Pei, J. *J. Am. Chem. Soc.* **2010**, *132*, 15872–15874.
- (2) Schoen, D. T.; Schoen, A. P.; Hu, L.; Kim, H. S.; Heilshorn, S. C.; Cui, Y. *Nano Lett.* **2010**, *10*, 3628–3632.
- (3) Li, Z.; Li, Q.; Fang, Y.; Wang, H.; Li, Y.; Wang, X. *J. Mater. Chem.* **2011**, *21*, 17185–17192.
- (4) Xia, Y.; Yang, P.; Sun, Y.; Wu, Y.; Mayers, B.; Gates, B.; Yin, Y.; Kim, F.; Yan, H. *Adv. Mater.* **2003**, *15*, 353–389.
- (5) Zhang, B.; Yu, X.; Ge, C.; Dong, X.; Fang, Y.; Li, Z.; Wang, H. *Chem. Commun.* **2010**, *46*, 9188–9190.
- (6) (a) Sun, Y.; Gates, B.; Mayers, B.; Xia, Y. *Nano Lett.* **2002**, *2*, 165–168.
- (7) Wang, H.; Li, Z.; Huang, Y.; Li, Q.; Wang, X. *J. Mater. Chem.* **2010**, *20*, 3883–3889.
- (8) Choi, J.; McDonough, J.; Jeong, S.; Yoo, J.; Chan, C.; Cui, Y. *Nano Lett.* **2010**, *10*, 1409–1413.
- (9) Wang, Y.; Song, S.; Shen, P.; Guo, C.; Li, C. *J. Mater. Chem.* **2009**, *19*, 6149–6153.
- (10) Chen, J.; Zhu, T.; Yang, X.; Yang, H.; Lou, X. *J. Am. Chem. Soc.* **2010**, *132*, 13162–13164.
- (11) Aricò, A. S.; Bruce, P.; Scrosati, B.; Tarascon, J. M.; Schalkwijk, W. V. *Nat. Mater.* **2005**, *4*, 366–377.
- (12) Guo, Y.; Hu, J.; Wan, L. *Adv. Mater.* **2008**, *20*, 2878–2887.
- (13) Liu, H.; Wang, G.; Liu, J.; Qiao, S.; Ahn, H. *J. Mater. Chem.* **2011**, *21*, 3046–3052.
- (14) Ge, M.; Rong, J.; Fang, X.; Zhou, C. *Nano Lett.* **2012**, *12*, 2318–2323.
- (15) Bai, F.; Sun, Z.; Wu, H.; Haddad, R.; Coker, E.; Huang, J.; Rodriguez, M.; Fan, H. *Nano Lett.* **2011**, *11*, 5196–5200.
- (16) Wang, P.; Bai, B.; Hu, S.; Zhuang, J.; Wang, X. *J. Am. Chem. Soc.* **2009**, *131*, 16953–16960.
- (17) Tsuruoka, T.; Furukawa, S.; Takashima, Y.; Yoshida, K.; Isoda, S.; Kitagawa, S. *Angew. Chem., Int. Ed.* **2009**, *48*, 4739–4743.
- (18) Xu, Y.; Al-Salim, N.; Bumby, C.; Tilley, R. *J. Am. Chem. Soc.* **2009**, *131*, 15990–15991.
- (19) Ning, J.; Men, K.; Xiao, G.; Wang, L.; Dai, Q.; Zou, B.; Liu, B.; Zou, G. *Nanoscale* **2010**, *2*, 1699–1703.
- (20) Jeffrey, R.; Brownson, C.; Claude, L. *Chem. Mater.* **2006**, *18*, 6397–6402.
- (21) Zhai, C.; Du, N.; Zhang, H.; Yu, J.; Yang, D. *ACS Appl. Mater. Interfaces* **2011**, *3*, 4067–4074.
- (22) Zhong, H.; Yang, G.; Song, H.; Liao, Q.; Cui, H.; Shen, P.; Wang, C. *J. Phys. Chem. C* **2012**, *116*, 9319–9326.
- (23) Li, Y.; Tu, J.; Huang, X.; Wu, H.; Yuan, Y. *Electrochim. Acta* **2006**, *52*, 1383–1389.
- (24) Kang, J.; Park, J.; Kim, D. *Electrochem. Commun.* **2010**, *12*, 307–310.
- (25) Lou, X.; Li, C.; Archer, L. A. *Adv. Mater.* **2009**, *21*, 2536–2539.
- (26) Guo, C.; Wang, M.; Chen, T.; Lou, X.; Li, C. *Adv. Energy Mater.* **2011**, *1*, 736–741.
- (27) Guo, C.; Shen, Y.; Dong, Z.; Chen, X.; Lou, X.; Li, C. *Energy Environ. Sci.* **2012**, *5*, 6919–6922.
- (28) Chan, C.; Peng, H.; Liu, G.; McIlwrath, K.; Zhang, X.; Huggins, R.; Cui, Y. *Nat. Nanotechnol.* **2008**, *3*, 31–35.
- (29) Jiang, J.; Liu, J.; Ding, R.; Ji, X.; Hu, Y.; Li, X.; Hu, A.; Wu, F.; Zhu, Z.; Huang, X. *J. Phys. Chem. C* **2010**, *114*, 929–932.
- (30) Sun, C.; Rajasekhara, S.; Goodenough, J.; Zhou, F. *J. Am. Chem. Soc.* **2011**, *133*, 2132–2135.
- (31) Aso, K.; Hayashi, A.; Tatsumisago, M. *Cryst. Growth Des.* **2011**, *11*, 3900–3904.

- (32) Price, L. S.; Parkin, I. P.; Hardy, A. M. E.; Clark, R. J. H. *Chem. Mater.* **1999**, *11*, 1792–1799.
- (33) Panda, S.; Datta, A.; Dev, A.; Gorai, S.; Chaudhuri, S. *Cryst. Growth Des.* **2006**, *6*, 2177–2181.
- (34) Dai, X.; Dayeh, S.; Veeramuthu, V.; Larrue, A.; Wang, J.; Su, H.; Soci, C. *Nano Lett.* **2011**, *11*, 4947–4952.
- (35) Dubrovskii, V.; Cirlin, G.; Sibirev, N.; Jabeen, F.; Harmand, J.; Werner, P. *Nano Lett.* **2011**, *11*, 1247–1253.
- (36) Fang, Y.; Wen, X.; Yang, S. *Angew. Chem.* **2006**, *118*, 4771–4774.
- (37) Qin, A.; Zhou, X.; Qiu, Y.; Fang, Y.; Su, C.; Yang, S. *Adv. Mater.* **2008**, *20*, 768–773.
- (38) Yang, S.; Ge, S.; Liu, Z.; Fang, Y.; Li, Z.; Kuang, D.; Su, C. *RSC Adv.* **2011**, *1*, 1691–1694.
- (39) Tian, L.; Zou, H.; Fu, J.; Yang, X.; Wang, Y.; Guo, H.; Fu, X.; Liang, C.; Wu, M.; Shen, P.; Gao, Q. *Adv. Funct. Mater.* **2010**, *20*, 617–623.
- (40) Zhang, Y.; Lu, J.; Shen, S.; Xu, X.; Wang, Q. *Chem. Commun.* **2011**, *47*, 5226–5228.
- (41) Sun, X.; Li, Y. *Angew. Chem., Int. Ed.* **2004**, *43*, 597–601.
- (42) Subramanian, V.; Burke, W.; Zhu, H.; Wei, B. *J. Phys. Chem. C.* **2008**, *112*, 4550–4556.